How capillarity affects the propagation of elastic waves in soft gels

P. Chantelot, L. Domino, and A. Eddi*

PMMH, CNRS, ESPCI Paris, Université PSL, Sorbonne Université, Université de Paris, F-75005 Paris, France

(Received 12 November 2019; accepted 4 March 2020; published 30 March 2020)

Elastic waves propagating at the interface of soft solids can be altered by the presence of external forces such as capillarity and gravity. We measure the dispersion relation of waves at the free surface of agarose gels with great accuracy, revealing the existence of multiple modes as well as an apparent dispersion. We disentangle the role of capillarity and elasticity by considering the three-dimensional nature of mechanical waves, achieving quantitative agreement between theoretical predictions and experiments. Notably, our results show that capillarity plays an important role for wave numbers smaller than expected from balancing elastic and capillary forces. We further confirm the efficiency of our approach by including the effect of gravity in our predictions and quantitatively comparing it to experiments.

DOI: 10.1103/PhysRevE.101.032609

I. INTRODUCTION

Mechanical waves propagating in biological tissues have been at the center of attention since the development of ultrasonic imaging more than 50 years ago [1]. Using soft materials to mimic the physics of wave propagation inside the body has enabled the development of technological innovations, such as elastography, allowing for direct measurement of the bulk elastic properties [2,3]. Soft solids have also been used as a model for fracture dynamics [4,5] and, in particular, for the role of friction and fault structure on rupture dynamics during earthquakes [6,7]. Wave propagation at interfaces raises the question of additional forces competing with elasticity. Indeed, solid interfaces possess a surface tension γ that dominates bulk elasticity at the small scale, below the elastocapillary length $\ell_{ec} = \gamma/\mu$, where μ is the solid shear modulus [8–10]. Depositing liquid drops on soft substrates allows one to probe the competition between elasticity and capillarity, as the wetting ridge induced by the contact line sets the drop's statics and dynamics [11]. For very soft solids, ℓ_{ec} can be as large as 1 mm. Capillary phenomena then become macroscopically visible at free surfaces: edges are rounded [12] and cylinders develop undulations reminiscent of the classical Plateau-Rayleigh instability for liquids [13]. Waves existing at the interface of soft materials have been only partially described so far. The existence of two regimes, dominated by elasticity or capillarity, theoretically predicted [14] and initially probed experimentally in the late 1990s [15], has been at the center of discussion [16,17]. Recent work focused on the transition between the two regimes, yet with limited experimental resolution [18]. In this article, we propose to combine accurate wave-field measurements and a theoretical analysis in order to discriminate the influence of capillarity on the propagation of mechanical waves at the free surface of soft gels.

II. EXPERIMENTAL SETUP

We make agarose gels by heating a solution of water and agarose (Sigma A4550-500G) at 95 °C. The solution is poured into a rectangular container (8.5 × 26 cm) and left to cool at room temperature for 2 h. We determine the rheology of the hydrogels for concentrations of 2 and 3 g/L, which gives shear moduli, μ, of 95 and 380 Pa, respectively (see Appendix A). We use the samples within 1 h after reticulation, so that evaporation does not affect their mechanical properties (see Appendix B). We generate plane waves at the air-gel interface by locally imposing a vertical sinusoidal motion with frequency f at the free surface of the sample. To do so, we deposit a rectangular source with dimensions 80 × 8 × 2 mm, which size does not influence the results (see Appendix C), on the surface of the gel and actuate it with an electromagnet, or alternatively we use a vibration exciter [Fig. 1(a)]. Several techniques have been used in the literature to measure surface waves including quasielastic surface light scattering [15], specular reflection spectroscopy [19,20], and the oscillatory response of a magnetic exciter [21]. The proposed methods are particularly adapted for short wavelengths, whereas here we want to measure extended wave fields with centimetric to millimetric wavelengths. We thus choose to measure the out-of-plane displacement field at the interface using a synthetic Schlieren imaging technique, based on the apparent displacement of a pattern caused by refraction at the surface [22]. We record from the top at a frame rate of 350 Hz for f ranging from 10 to 160 Hz. We use sweeps at a rate of 1.6 Hz/s, small enough to consider the excitation as monochromatic when analyzing small signal windows.

III. DISPERSION RELATION

We show in Fig. 1(b) a typical height field obtained at $f = 40$ Hz in a gel with $\mu = 95$ Pa and depth $h = 1.1 \pm 0.1$ cm. We extract the wave field at any frequency by Fourier filtering a signal window around the corresponding f. We then use spatial two-dimensional (2D) Fourier transforms to extract the

*antonin.eddi@espci.fr

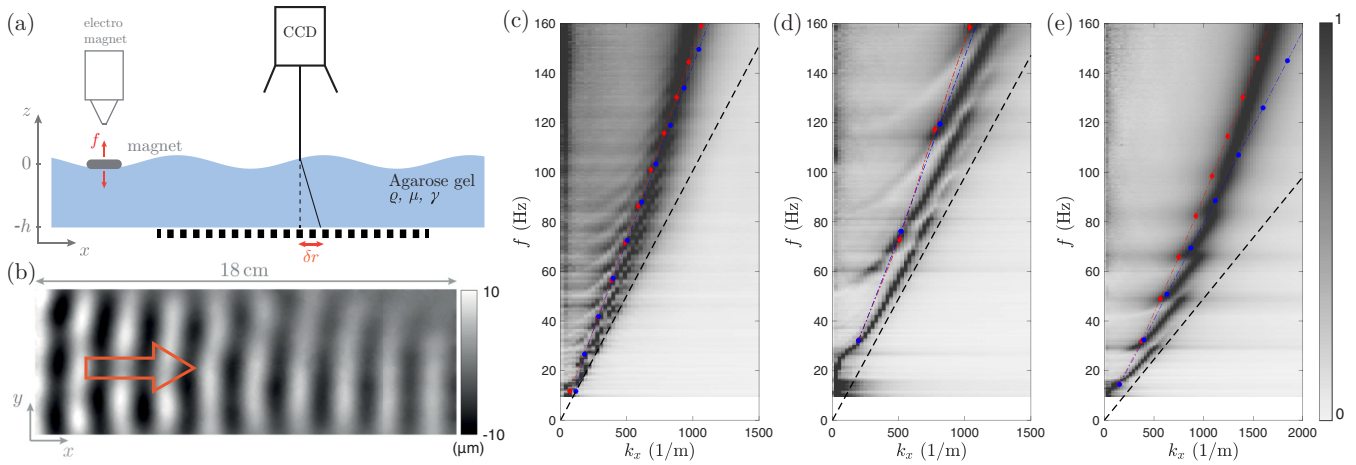

FIG. 1. (a) Sketch of the experimental setup using synthetic Schlieren imaging [22]. (b) Height field obtained for $f = 40$ Hz in a gel with $\mu = 95$ Pa and $h = 1.1 \pm 0.1$ cm. The source is on the left and the red arrow shows the direction of propagation. (c–e) Dispersion relations measured at the gel interface; the wave number is measured along the x axis. Dashed black lines show the dispersion relation of shear waves: $\omega = k\sqrt{\mu/\rho}$. Red and blue symbols represent the maximum of the normalized out-of-plane displacement along each mode predicted by Eq. (1) with and without taking into account capillarity, respectively. (c) $\mu = 380$ Pa, $h = 3.4 \pm 0.4$ cm. (d) $\mu = 380$ Pa, $h = 1.1 \pm 0.1$ cm. (e) $\mu = 95$ Pa, $h = 1.1 \pm 0.1$ cm.

spectra along the propagation direction, which we normalize by their maximum amplitude. By stacking the spectra obtained at each f, we can construct a dispersion relation map, which we show in Fig. 1(c) for a gel with $\mu = 380$ Pa and thickness $h = 3.4 \pm 0.4$ cm. It shows the coexistence of two distinct behaviors. (i) For $f < 120$ Hz, we observe multiple branches, which start at increasing cutoff frequencies. (ii) At higher frequencies, the branches merge, and a single line is observed. We interpret the presence of several cutoff frequencies (at $k_x = 0$) as a signature of the finite thickness: in a confined sample the vertical component of the wave vector can only take discrete values. We investigate this effect by decreasing h to 1.1 ± 0.1 cm while keeping μ constant [Fig. 1(d)]. We observe the strong effect of the depth: there still are several branches, but with markedly different cutoff frequencies. The fundamental mode appears at higher frequencies, and the following branches begin to exist at larger f and are farther apart. Then we probe the effect of the gel's elastic properties by decreasing the agarose concentration to obtain a gel with $\mu = 95$ Pa and $h = 1.1$ cm [Fig. 1(e)]. The cutoff frequencies are now lower. We note that the local slope of each branch is significantly smaller than that of the stiffer gels [Figs. 1(c) and 1(d)]. The plots in Figs. 1(c)–1(e) of the dispersion relation of shear waves $\omega = k\sqrt{\mu/\rho}$ (dashed black lines) [23] suggest that this local slope is controlled by the speed of elastic shear waves. Conversely, the slope of the single line observed at higher frequencies is larger than that of shear waves. The dispersion relation can be regarded as an apparent dispersion curve whose group velocity progressively increases. The latter effect and the increase in the local slope of the branches at high k in the softer gel [Fig. 1(e)] both hint at the presence of capillarity, which could stiffen the interface at large k.

IV. IN-DEPTH DISPLACEMENTS

Surface measurements suggest that the finite thickness selects the modes at low f. We confirm this hypothesis by measuring in-depth displacement fields. We seed the gel with microparticles (diameter, ~ 10 μm; density, 1100 kg/m^3) and illuminate the xz plane with a laser sheet [Fig. 2(a)]. We use a low microparticle concentration, $\chi = 0.14\%$, so that the inclusions do not modify the gel elastic properties (see Appendix D). We measure the local displacement field at 250 fps, using a standard digital image correlation algorithm [24], in a window with dimensions of 1.8×1.6 cm approximately 2 cm away from the source. Figures 2(b) and 2(c) present a quiver plot of the displacement vector superimposed over a map of its magnitude for a gel with $\mu = 95$ Pa and $h = 1.9 \pm 0.1$ cm excited at $f = 40$ Hz [Fig. 2(b)] and $f = 120$ Hz [Fig. 2(c)]. The displacement amplitude is of the order of 10 μm, and both vertical and horizontal components are present. At $f = 40$ Hz we observe displacements in the entire sample, without a significant decay in the vertical direction, while at $f = 120$ Hz the amplitude seems to decrease more rapidly in the vertical than in the horizontal direction. We extract the spatial spectra corresponding to these displacements fields [Figs. 2(d) and 2(e)]. For both frequencies, the wave vectors have a nonzero component on the vertical axis: the previous surface measurements correspond to their horizontal projection. The norm of the wave vector is $||\mathbf{k}|| = 981$ 1/m for $f = 40$ Hz and $||\mathbf{k}|| = 2768$ 1/m for $f = 120$ Hz, two values compatible with the propagation of shear waves in the bulk ($\omega = k\sqrt{\mu/\rho}$). Yet the two spectra are markedly different. For $f = 40$ Hz, we observe two peaks that correspond to the presence of an incident ($k_z < 0$) and a reflected ($k_z > 0$) wave created by the reflection at the bottom of the tank. We evidence this result by plotting in Fig. 2(f) the wave fields obtained by taking the inverse Fourier transform of each peak. At a higher frequency ($f = 120$ Hz), the spatial spectrum shows only one peak [Fig. 2(d)]. The wave traveling downwards is damped before it reaches $z = -h$, so that propagation occurs mostly at the surface. These experiments confirm that the multiple modes observed at low frequencies result from the vertical confinement and they suggest that, at

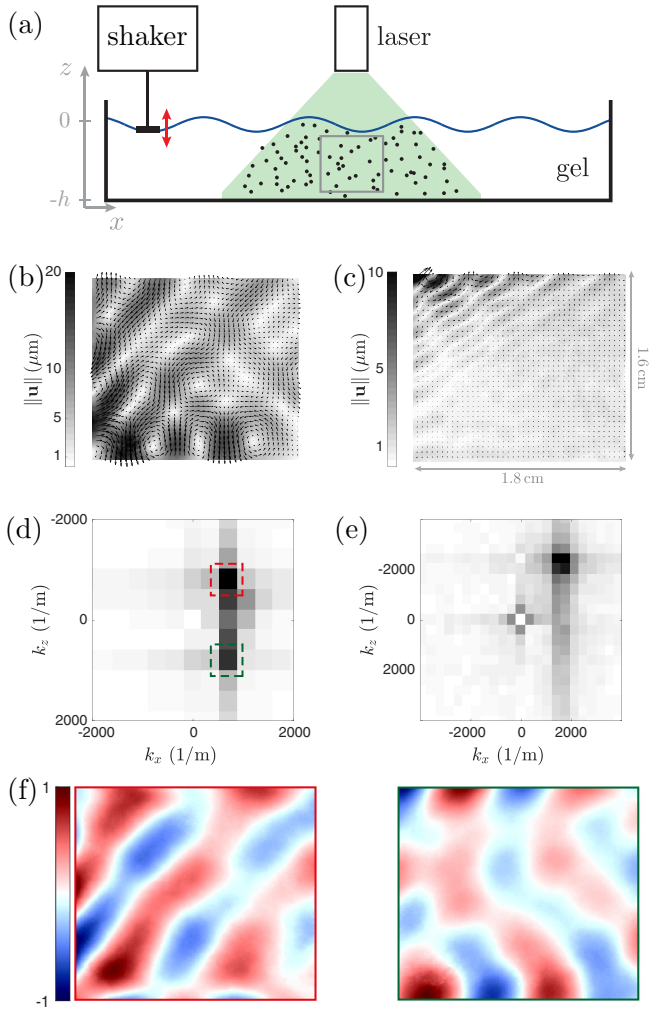

FIG. 2. (a) Sketch of the digital image correlation experimental setup used to measure in-depth displacement fields. (b, c) Displacement field inside a gel with $\mu = 95$ Pa and $h = 2.3 \pm 0.3$ cm for $f = 40$ Hz (b) and $f = 120$ Hz (c). (d, e) Spatial spectra corresponding to the fields in (b) and (c). The two peaks in (d) correspond to the presence of an incident wave and its reflection at the bottom of the tank. (f) Wave fields obtained by taking the inverse Fourier transform of each peak in (b).

high frequencies, dissipation prevents the incident wave from propagating all the way down to the bottom of the sample.

V. MODELING

We now model wave propagation in soft materials. To account for our experimental observations, we address the case of vertically confined samples. We extend a previous analysis [16], which treated the case of a semi-infinite solid subjected to elastic and capillary forces, to a finite-thickness sample and add the contribution of gravity. We consider plane waves propagating along the x direction in an infinite 2D plate of thickness h and density ρ with elastic properties characterized by the Lamé coefficients λ and μ. We separate the displacement field $\boldsymbol{u}$ in a longitudinal curl-free contribution $\boldsymbol{u}_l$ and in a transverse divergence-free contribution $\boldsymbol{u}_t$. The longitudinal part can be described by a scalar potential Φ and the transverse part by a vector potential $\boldsymbol{H}$:

$$\boldsymbol{u} = \boldsymbol{u}_l + \boldsymbol{u}_t = \nabla\Phi + \nabla \times \boldsymbol{H}.$$

Both Φ and H_y verify a wave equation [23],

$$\nabla^2\Phi - \frac{1}{c_l^2}\frac{\partial^2\phi}{\partial t^2} = 0, \quad \nabla^2 H_y - \frac{1}{c_t^2}\frac{\partial^2 H_y}{\partial t^2} = 0,$$

where $c_t = \sqrt{\frac{\mu}{\rho}}$ and $c_l = \sqrt{\frac{\lambda+2\mu}{\rho}}$ are, respectively, the shear and longitudinal wave speeds. We seek solutions of the form $\Phi = f(z)e^{i(kx-\omega t)}$ and $H_y = ih(z)e^{i(kx-\omega t)}$, where we use k as k_x and impose the following boundary conditions. (i) At the bottom of the sample, the gel is bounded to the container, so that

$$u_x(z=-h) = u_z(z=-h) = 0.$$

(ii) At the free surface, assuming small deformations to linearize the boundary conditions at $z = 0$ and taking advantage of the incompressibility of the hydrogels ($c_l \to \infty$), which allows the absorption of bulk gravity into the hydrostatic pressure, we impose

$$\sigma_{xz}(z=0) = 0, \quad \sigma_{zz}(z=0) = \gamma\frac{\partial^2 u_z}{\partial x^2} - \rho g u_z.$$

Only the boundary condition at the interface sets this problem apart from the purely elastic one: capillarity and gravity are taken into account by relating the Laplace and hydrostatic pressure, respectively, to the normal stress. Using the four boundary conditions and substituting Φ and H_y, we obtain the dispersion relation for the gravitoelastocapillary waves (see Appendix E). This relation can be written in dimensionless form by introducing the variables $\tilde{k} = kh$ and $\tilde{\omega} = \omega h/c_t$:

$$\begin{aligned}&\tilde{k}^2 \sinh\tilde{\alpha}\sin\tilde{\beta}((\tilde{k}^2-\tilde{\beta}^2)^2 + 4\tilde{\alpha}^2\tilde{\beta}^2)\\ &\quad - \tilde{\alpha}\tilde{\beta}\cosh\tilde{\alpha}\cos\tilde{\beta}(4\tilde{k}^4 + (\tilde{k}^2-\tilde{\beta}^2)^2)\\ &\quad + 4\tilde{\alpha}\tilde{\beta}\tilde{k}^2(\tilde{k}^2-\tilde{\beta}^2) - \left(\Gamma + \frac{G}{\tilde{k}^2}\right)\tilde{\alpha}\tilde{k}^2(\tilde{k}^2+\tilde{\beta}^2)\\ &\quad \times (\tilde{k}^2\cosh\tilde{\alpha}\sin\tilde{\beta} + \tilde{\alpha}\tilde{\beta}\sinh\tilde{\alpha}\cos\tilde{\beta}) = 0, \qquad (1)\end{aligned}$$

where $\tilde{\alpha}^2 = -\tilde{k}^2$ and $\tilde{\beta}^2 = \tilde{\omega}^2 - \tilde{k}^2$. We identify two dimensionless parameters, $\Gamma = \gamma/\mu h$ and $G = \rho g h/\mu$, which compare the elastocapillary length $\ell_{ec} = \gamma/\mu$ and the elastogravity length $\ell_{eg} = \mu/\rho g$ to the thickness h. Using a secant method algorithm, we determine the zeros in Eq. (1) (assuming that the surface tension of the gels is similar to that of water, i.e., $\gamma = 70$ mN/m). In Figs. 3(a)–3(c), we overlay the obtained curves (red lines) on experimental maps where the thickness of the sample was precisely controlled [so that μ is the only adjustable parameter in Eq. (1)]. The model is in good agreement with the measured data: it captures the existence of multiple branches and their cutoff frequencies and local slopes when varying both μ and h. The values μ_{th} used to fit the predicted relations to the experimental data are always larger than the expected μ. We qualitatively ascribe this discrepancy to the evaporation of the hot agarose solution during preparation [25]. Yet we do not explain the apparent dispersion: the signal is localized on a finite part of the predicted branches. We gain more insight by deriving the

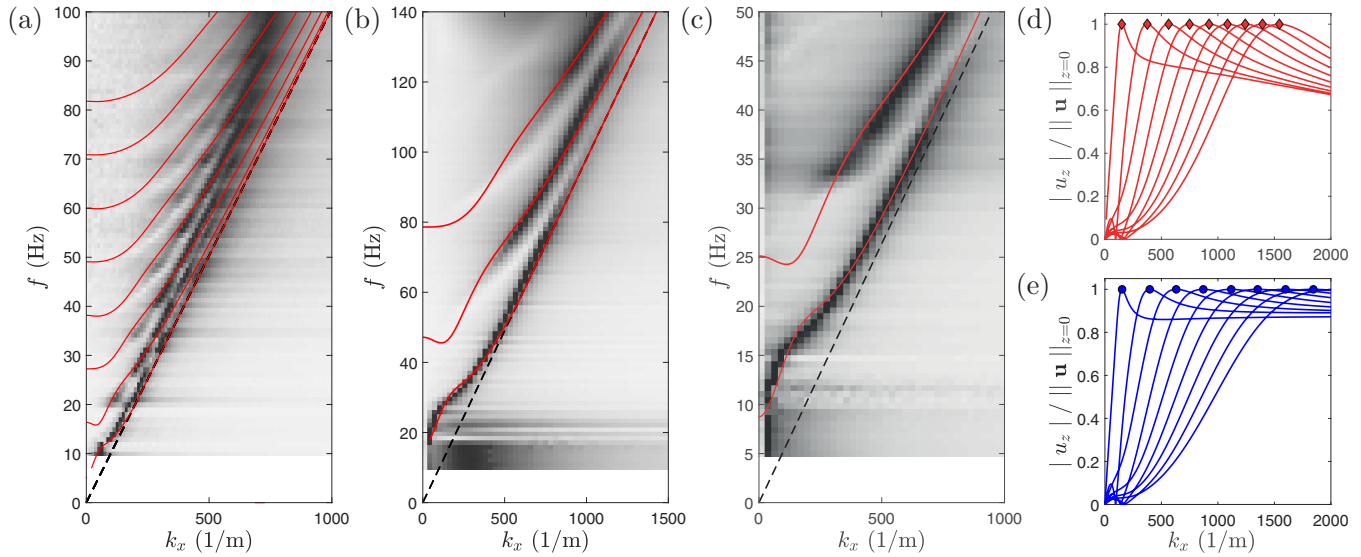

FIG. 3. (a–c) Overlay of the dispersion maps measured on samples with different μ and h values and the dispersion curves obtained by computing the zeros in Eq. (1) (μ_{th} being the only adjustable parameter). Dashed lines show the dispersion relation of shear waves: $\omega = k\sqrt{\mu/\rho}$. (a) $\mu = 380\,\text{Pa}$, $h = 2.90 \pm 0.05\,\text{cm}$, $\mu_{\text{th}} = 400\,\text{Pa}$ (b) $\mu = 380\,\text{Pa}$, $h = 0.98 \pm 0.05\,\text{cm}$, $\mu_{\text{th}} = 380\,\text{Pa}$, and (c) $\mu = 95\,\text{Pa}$, $h = 0.99 \pm 0.05\,\text{mm}$, $\mu_{\text{th}} = 110\,\text{Pa}$. (d, e) Normalized vertical displacement $|u_z|/||\mathbf{u}||$ as a function of k for $\mu_{\text{th}} = 120\,\text{Pa}$ and $h_{\text{th}} = 1.3\,\text{cm}$ with (d; red lines) and without (e; blue lines) taking capillarity into account.

displacement field associated with each mode: for any (ω, k) verifying Eq. (1), we can compute the displacement field at the interface up to a multiplicative constant (see Appendix E). We plot in Fig. 3(d) the norm of the vertical displacement normalized by the magnitude of the displacement vector at the interface, $|u_z|/||\mathbf{u}||_{z=0}$, as a function of k (red lines) for $\mu_{\text{th}} = 120\,\text{Pa}$ and $h_{\text{th}} = 1.3\,\text{cm}$. The normal displacement at $z = 0$ varies in a similar fashion for each mode: it increases sharply until it reaches a maximum for $k = k_m$ (red diamonds) and then decreases at a slower rate. As synthetic Schlieren imaging only detects out-of-plane motion, we expect to measure waves only when $k > k_m$ and that the signal intensity decays along each mode as k increases. The red symbols in Figs. 1(c)–1(e) represent the couples (ω_m, k_m) obtained from the model for each sample. Our prediction now captures the apparent dispersion; the red diamonds act as lower bounds for the presence of signal for each mode. The blurring of the modes into a single line can be qualitatively explained by the significant effect of dissipation at high frequencies, an effect that deserves a separate study.

VI. ELASTOCAPILLARY EFFECT

Although the shape of the apparent dispersion suggests that it is caused by surface tension, balancing the capillary-induced stress, of order γk, with the elastic stress predicts that capillarity dominates when $k > 2\pi/\ell_{\text{ec}} = 8.5 \times 10^3\ \text{m}^{-1}$ (for $\mu = 95\,\text{Pa}$), much larger than the wave numbers probed experimentally. We report in Fig. 3(e) the normalized vertical displacement at the interface for the same parameters as in Fig. 3(d) without taking into account the surface tension to evidence its role. The variations of the out-of-plane displacement are different when $k > k_m$, where we now observe a plateau. The nature of the displacement fields is modified, reducing the relative weight of the out-of-plane contribution. Physically, an extra energetic contribution due to capillarity tends to favor in-plane displacements even for $k < 2\pi/\ell_{\text{ec}}$. We also note that the values of (ω_m, k_m) are shifted so that we no longer recover the apparent dispersion in Figs. 1(c)–1(e) (blue circles): they align on a line with slope $\sqrt{2}c_t$, corresponding to Lamé modes (see Appendix F). This shows that the apparent dispersion is caused by capillarity for wave numbers lower than $2\pi/\ell_{\text{ec}}$. Since Γ ranges from 0.001 to 0.08 in the experiments in Fig. 1 and Fig. 3, the shape of the predicted modes is hardly modified by capillarity. To probe the effect of capillarity on the dispersion curves, we investigate wave propagation in a very shallow sample ($\Gamma \sim 1/h$). We report in Fig. 4(a) the dispersion relation of a gel with $\mu = 95\,\text{Pa}$ and $h = 0.23 \pm 0.05\,\text{cm}$ for which $\Gamma = 0.4$. The red lines represent the prediction of Eq. (1) with (solid line) and without (dashed line) capillary effects. The prediction lies closer to the experimental result when capillarity is included, which confirms its direct influence. It is noteworthy that the two effects discusssed above are specific to finite-thickness configurations and are markedly different from the elastic-to-capillary transition discussed in [15] and [18].

VII. ELASTOGRAVITY EFFECT

Finally, we check the influence of gravity on the dispersion relation. We characterize a sample whose interface normal points upwards or downwards. In the first case, gravity acts as a restoring force on the free interface, whereas in the second it tends to deform it and can even make it unstable [26,27]. Figures 3(c) and 4(b) present the dispersion relations obtained for a sample with $\mu = 95\,\text{Pa}$ and $h = 0.99 \pm 0.05\,\text{cm}$ when the interface points up or down, respectively. For such a sample $|G| = 1.02$, so that we expect gravitational forces to matter but remain below the instability threshold. The model accurately predicts the influence of gravity as shown by the

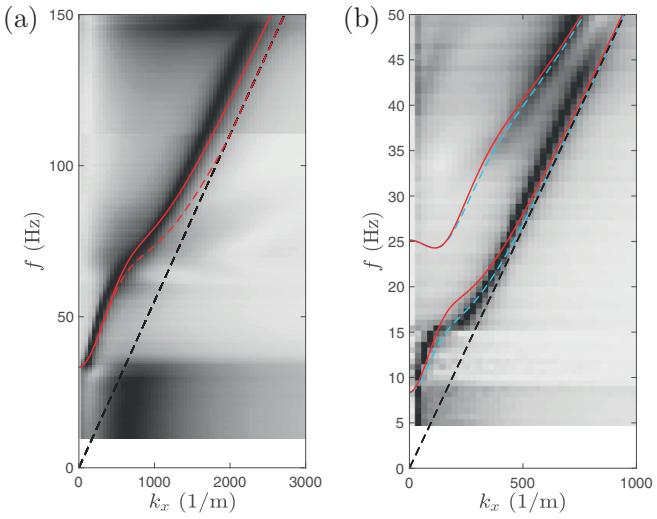

FIG. 4. (a) Dispersion map obtained for $\mu = 95\,\mathrm{Pa}$ and $h = 0.23 \pm 0.05\,\mathrm{cm}$. The solid red (dashed red) line represents the prediction of Eq. (1) ($\mu_{\mathrm{th}} = 120\,\mathrm{Pa}$, $h_{\mathrm{th}} = 0.26\,\mathrm{cm}$) with (without) including capillarity. (b) Dispersion map for $\mu = 95\,\mathrm{Pa}$ and $h = 0.99 \pm 0.05\,\mathrm{cm}$ when the interface points downwards. The solid red (dashed cyan) line corresponds to the prediction of Eq. (1) ($\mu_{\mathrm{th}} = 110\,\mathrm{Pa}$) with the interface pointing up (down). Dashed black lines show the dispersion relation of shear waves: $\omega = k\sqrt{\mu/\rho}$.

overlay of the solid red line (dashed cyan line) corresponding to the prediction of Eq. (1) ($\mu_{\mathrm{th}} = 110\,\mathrm{Pa}$) with the free surface pointing up (down). This shows that by tuning G below the value of the instability threshold, we can control the dispersion of the fundamental mode.

VIII. DISCUSSION

In this article, we use state-of-the-art measurement techniques to probe the propagation of surface waves in agarose gels with great accuracy, revealing the importance of finite thickness, which leads to the occurrence of multiple modes at low frequencies as well as the existence of an apparent dispersion. We quantitatively predict the dispersion relation using an elastic model including capillary forces. In particular, we capture the role of capillarity even at wave numbers lower than expected from scaling arguments in finite-thickness configurations through an intricate balance between in-plane and out-of-plane interfacial displacements and in very thin samples. We confirm the validity of our approach by including gravity in the model and successfully testing it against experimental data. The influence of gravity opens new perspectives: G can be tuned to create materials in which the phase and group velocity have opposite signs, a sought-after property allowing perfect lensing [28]. Furthermore, G also depends on the depth, enabling us to tune the medium properties down to subwavelength scales to create elastic metamaterials [29].

ACKNOWLEDGMENTS

We thank Sander Wildeman, Claire Prada, and Jacco Snoeijer for insightful discussions. P.C. and A.E. thank David Quéré for his support.

P.C. and L.D. contributed equally to this work.

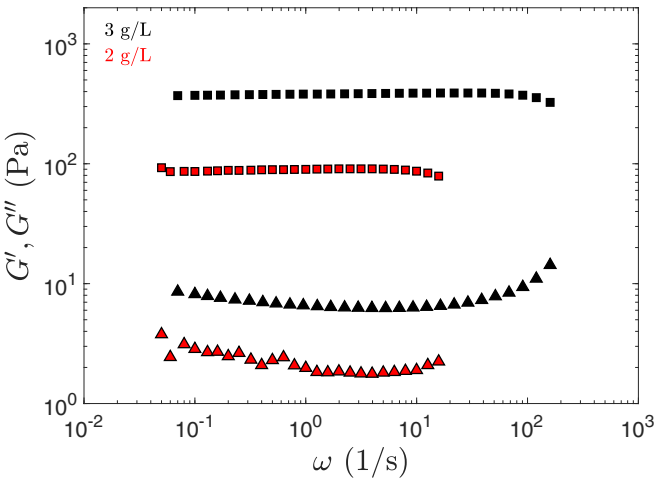

FIG. 5. Storage (G'; squares) and loss (G''; triangles) moduli of agar hydrogels with concentrations of 2 and 3 g/L plotted as a function of the pulsation ω.

APPENDIX A: RHEOLOGY MEASUREMENTS

We determine the rheology of the gels using a rheometer (Anton-Paar MCR501) in a plate-plate configuration. We measure the shear modulus $\mu(\omega) = G' + iG''$ for pulsations ranging from 0.05 to 100 rad/s at a fixed strain of 0.1% and report the results in Fig. 5. In the probed range, both G' and G'' are constant and G' is typically one order of magnitude larger than G''.

APPENDIX B: ROLE OF EVAPORATION

Drying, and more generally aging, is a major concern in hydrogels. We use our gels just after reticulation is complete and the gel has reached room temperature. A measurement typically takes less than 1 h and gels are discarded after they are measured. We are thus confident that there is no macroscopic skin at the gel surface, but there might be a small gradient of properties due to the slow drying occurring after the gel preparation. As an independent check, we measured the dispersion relation of a gel sample: within 1 h of reticulation [Fig. 6(a)], 1 h after the first measurement [Fig. 6(b)], and 3 h after the first measurement [Fig. 6(c)]. We observe no significant change between the dispersion relations in Figs. 6(a) and 6(b) [except for an input signal error between 35 and 55 Hz in Fig. 6(a)]. Yet we note, in Fig. 6(c), an increase in the local slope of the branches, an observation compatible with an increase in the gel shear modulus, which can be attributed to evaporation. Although evaporation occurs in our system, it is not a limiting parameter in our experiments.

APPENDIX C: FINITE SOURCE SIZE

The finite size of the actuator could have an influence on the results. Indeed, the measured wave fields depend on both the response of the material and the ability of the source to generate waves at a given frequency. We probed the effect of source size by using two PMMA strips of different widths. Figures 6(d) and 6(e) show the dispersion relations for a gel with $\mu = 380\,\mathrm{Pa}$ and $h = 9.8\,\mathrm{mm}$ obtained by using actuators

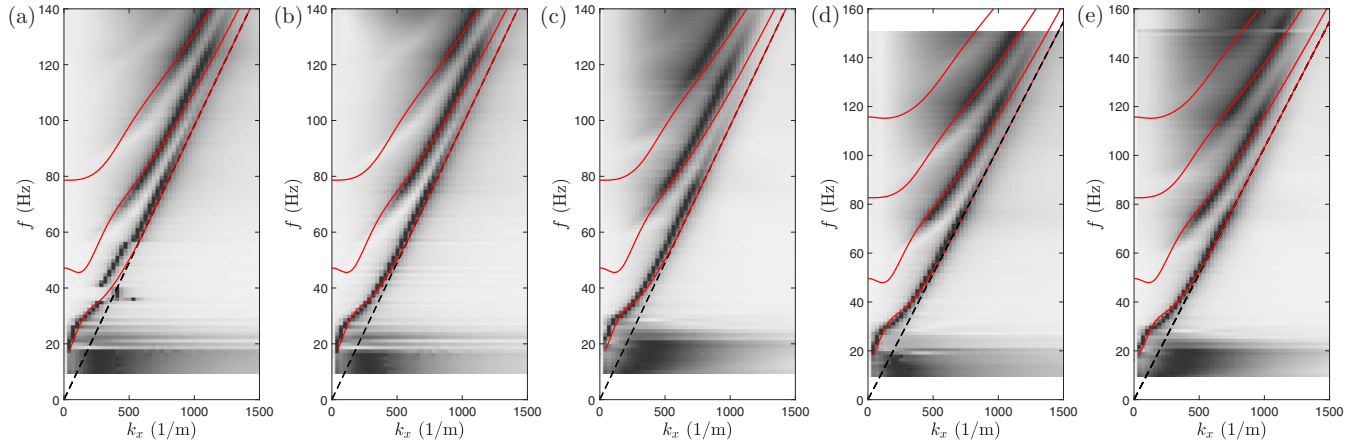

FIG. 6. Dispersion relation measured from a gel with $\mu = 380\,\text{Pa}$ and $h = 0.98 \pm 0.05\,\text{cm}$ (a) within 1 h of reticulation and (b) 1 h after and (c) 3 h after the first measurement. Red curves are obtained from Eq. (1) in the text with $\mu_{\text{th}} = 380\,\text{Pa}$. (d, e) Overlay of the dispersion maps for a gel with $\mu = 380\,\text{Pa}$ and $h = 9.8\,\text{mm}$ and dispersion curves predicted from Eq. (1) in the text ($\mu_{\text{th}} = 420\,\text{Pa}$) for actuators with widths of 4.5 mm (d) and 14 mm (e).

with widths of 4.5 and 14 mm. The two dispersion relations are almost identical, showing that our results are independent of the size of the actuator in the range of parameters that we consider.

APPENDIX D: EFFECT OF INCLUSIONS

The presence of microparticles can modify the material properties of the gels. We extracted the particle concentration from digital image correlation images by binarizing the image to find the area corresponding to bright pixels. Knowing the thickness of the sheet ($\simeq 200\ \mu$m) and the size of the particles ($\simeq 10\ \mu$m), we obtain the particle concentration $\chi = 0.14\%$. We deduce the density of the gel with inclusions, $\rho_{\text{eff}} = (1-\chi)\rho + \chi\rho_p = 1000\ \text{kg/m}^3$. Then we determine the effect of the inclusions on the gel shear modulus using Eshelby theory [30]. We assume that the inclusions are rigid, as the shear modulus of the particles is much larger than that of the gel. The effective shear modulus, μ_{eff}, in the case of dilute spherical inclusions is given by $\mu_{\text{eff}} = \mu(1 - B\chi)$, where $B = -15(1-\nu)/(2(4-5\nu))$, with ν the Poisson ratio. For the results shown in Fig. 2 ($\mu = 95\,\text{Pa}$, $\nu = 0.5$), we get $\mu_{\text{eff}} = 95.3\,\text{Pa}$. The presence of the inclusions has a negligible effect on the density and shear modulus of the gel. We do not expect the results to be modified and neglect their influence.

APPENDIX E: MODELING: DERIVATION OF THE DISPERSION RELATION AND OF THE DISPLACEMENT FIELD

We consider plane waves propagating along the x direction in an infinite 2D plate of thickness h and density ρ whose elastic properties are characterized by the Lamé coefficients λ and μ. We use Helmholtz theorem to separate the displacement field $\boldsymbol{u}$ in a longitudinal curl-free contribution $\boldsymbol{u}_l$ and in a transverse divergence-free contribution $\boldsymbol{u}_t$. The longitudinal part can be described by a scalar potential Φ and the transverse part by a vector potential $\boldsymbol{H}$:

$$\boldsymbol{u} = \boldsymbol{u}_l + \boldsymbol{u}_t = \nabla\Phi + \nabla \times \boldsymbol{H}.$$

Both Φ and H_y verify a wave equation [23],

$$\nabla^2\Phi - \frac{1}{c_l^2}\frac{\partial^2\phi}{\partial t^2} = 0, \quad \nabla^2 H_y - \frac{1}{c_t^2}\frac{\partial^2 H_y}{\partial t^2} = 0,$$

where $c_t = \sqrt{\frac{\mu}{\rho}}$ and $c_l = \sqrt{\frac{\lambda+2\mu}{\rho}}$ are, respectively, the shear and longitudinal wave speeds. We look for solutions of the form $\Phi = f(z)e^{i(kx-\omega t)}$ and $H_y = ih(z)e^{i(kx-\omega t)}$, where we write k in place of k_x. By substitution in the wave equations, we obtain

$$\frac{\partial^2 f}{\partial z^2} + \alpha^2 f = 0, \quad \frac{\partial^2 h}{\partial z^2} + \beta^2 h = 0,$$

where $\alpha^2 = \frac{\omega^2}{c_l^2} - k^2$ and $\beta^2 = \frac{\omega^2}{c_t^2} - k^2$. We deduce the form of the solution of f and h and write the expressions for u_x and u_z:

$$\begin{aligned} u_x &= i[k(A\sin\alpha z + B\cos\alpha z) \\ &\quad + \beta(C\cos\beta z - D\sin\beta z)]e^{i(kx-\omega t)}, \\ u_z &= [\alpha(A\cos\alpha z - B\sin\alpha z) \\ &\quad + k(C\sin\beta z + D\cos\beta z)]e^{i(kx-\omega t)}. \end{aligned}$$

From the displacements, we obtain the stresses σ_{xz} and σ_{zz}:

$$\sigma_{xz} = \rho c_t^2\left(\frac{\partial u_x}{\partial z} + \frac{\partial u_z}{\partial x}\right),$$

$$\sigma_{zz} = \rho c_l^2\frac{\partial u_z}{\partial z} + \rho\left(c_l^2 - 2c_t^2\right)\frac{\partial u_x}{\partial x}.$$

We have now determined all quantities to express the boundary conditions. At the bottom of the sample, we assume that the gel is bound to the container:

$$u_x(z=-h) = u_z(z=-h) = 0.$$

At the free surface, assuming small deformations to linearize the boundary conditions at $z = 0$ and taking advantage of the incompressibility of the hydrogels ($c_l \to \infty$), which allows us

to compensate gravity by a pressure field, we impose

$$\sigma_{xz}(z=0)=0, \quad \sigma_{zz}(z=0)=\gamma\frac{\partial^2 u_z}{\partial x^2}-\rho g u_z.$$

The four boundary conditions yield four equations, involving the constants A, B, C, and D, which can be recast in matrix form:

$$\begin{bmatrix} -k\sin\alpha h & k\cos\alpha h & \beta\cos\beta h & \beta\sin\beta h \\ \alpha\cos\alpha h & \alpha\sin\alpha h & -k\sin\beta h & k\cos\beta h \\ 2k\alpha & 0 & 0 & k^2-\beta^2 \\ k^2\alpha(\gamma+\rho g/k^2) & \rho c_t^2(k^2-\beta^2) & 2\rho c_t^2 k\beta & k^3(\gamma+\rho g/k^2) \end{bmatrix}\cdot\begin{bmatrix} A \\ B \\ C \\ D \end{bmatrix}=0.$$

Waves propagate when there are nontrivial solutions to the above system; the dispersion relation is obtained by taking the determinant of the matrix. This relation can be written in dimensionless form by introducing the variables $\tilde{k}=kh$ and $\tilde{\omega}=\omega h/c_t$, allowing one to obtain Eq. (1). For any couple (ω, k) that verifies the dispersion relation, we obtain the values of three of the constants A, B, C, and D, allowing us to determine the displacement field up to a constant. We give the values of A, B, and C as a function of D:

$$C=-D\frac{k^2-\beta^2+\alpha\beta e^{i\beta h}(e^{-i\alpha h}-e^{i\alpha h})-k^2e^{i\beta h}(e^{-i\alpha h}+e^{i\alpha h})}{k^2-\beta^2-\alpha\beta e^{-i\beta h}(e^{-i\alpha h}-e^{i\alpha h})-k^2e^{-i\beta h}(e^{-i\alpha h}+e^{i\alpha h})},$$

$$A=-\frac{1}{ik(e^{-i\alpha h}+e^{i\alpha h})}\left(C\left(\frac{k^2-\beta^2}{2\alpha}e^{i\alpha h}-\beta e^{-i\beta h}\right)+D\left(\frac{k^2-\beta^2}{2\alpha}e^{i\alpha h}+\beta e^{i\beta h}\right)\right), \quad B=A+i\frac{(\beta^2-k^2)(C+D)}{2\alpha k}.$$

APPENDIX F: LAMÉ MODES

Lamé modes are a special solution of the Rayleigh-Lamb equation obtained when $\omega=\sqrt{2}kc_t$. They correspond to the propagation of pure bulk shear waves at a 45° angle with the plate axis and to the maximum of normal displacement at the surface of the plate [31]. One can show by substituting the expression of Lamé modes in Eq. (1) that it reduces to the Rayleigh-Lamb equation for symmetric modes of a plate of thickness $2h$ in the absence of capillarity and gravity. Thus, the maxima of the normal displacement at the free surface of the gels align on a line with slope $\sqrt{2}c_t$ when we do not take surface tension into account.

[1] J. J. Wild and J. M. Reid, Science **115**, 226 (1952).
[2] L. Sandrin, S. Catheline, M. Tanter, X. Hennequin, and M. Fink, Ultrason. Imag. **21**, 259 (1999).
[3] J. Bercoff, M. Tanter, and M. Fink, IEEE Trans. Ultrason. Ferroelect. Freq. Control **51**, 396 (2004).
[4] D. Bonn, H. Kellay, M. Prochnow, K. Ben-Djemiaa, and J. Meunier, Science **280**, 265 (1998).
[5] A. Livne, G. Cohen, and J. Fineberg, Phys. Rev. Lett. **94**, 224301 (2005).
[6] S. Latour, T. Gallot, S. Catheline, C. Voisin, F. Renard, E. Larose, and M. Campillo, Europhys. Lett. **96**, 59003 (2011).
[7] S. Latour, C. Voisin, F. Renard, E. Larose, S. Catheline, and M. Campillo, J. Geophys. Res.: Solid Earth **118**, 5888 (2013).
[8] J. H. Snoeijer, Phys. Rev. Fluids **1**, 060506 (2016).
[9] R. W. Style, A. Jagota, C.-Y. Hui, and E. R. Dufresne, Annu. Rev. Condens. Matter Phys. **8**, 99 (2017).
[10] J. Bico, É. Reyssat, and B. Roman, Annu. Rev. Fluid Mech. **50**, 629 (2018).
[11] B. Andreotti and J. H. Snoeijer, Annu. Rev. Fluid Mech. **52**, 285 (2019).
[12] C. Hui, A. Jagota, Y.-Y. Lin, and E. Kramer, Langmuir **18**, 1394 (2002).
[13] S. Mora, T. Phou, J.-M. Fromental, L. M. Pismen, and Y. Pomeau, Phys. Rev. Lett. **105**, 214301 (2010).
[14] J. L. Harden, H. Pleiner, and P. A. Pincus, J. Chem. Phys. **94**, 5208 (1991).
[15] F. Monroy and D. Langevin, Phys. Rev. Lett. **81**, 3167 (1998).
[16] Y. Onodera and P.-K. Choi, J. Acoust. Soc. Am. **104**, 3358 (1998).
[17] K. Ahn, K. H. Yoon, and M. W. Kim, Europhys. Lett. **54**, 199 (2001).
[18] X. Shao, J. R. Saylor, and J. B. Bostwick, Soft Matter **14**, 7347 (2018).
[19] A. Tay, C. Thibierge, D. Fournier, C. Frétigny, F. Lequeux, C. Monteux, J.-P. Roger, and L. Talini, Rev. Sci. Instrum. **79**, 103107 (2008).
[20] B. Pottier, G. Ducouret, C. Fretigny, F. Lequeux, and L. Talini, Soft Matter **7**, 7843 (2011).
[21] E. Rolley, J. H. Snoeijer, and B. Andreotti, Rev. Sci. Instrum. **90**, 023906 (2019).
[22] S. Wildeman, Exp. Fluids **59**, 97 (2018).
[23] L. D. Landau and E. M. Lifshitz, *Theory of Elasticity*, 3rd ed., Course of Theoretical Physics Vol. 7 (Butterworth-Heinemann, 1986).
[24] J. Blaber, B. Adair, and A. Antoniou, Exp. Mech. **55**, 1105 (2015).
[25] Evaporation occurs over larger surfaces in the samples than during rheology measurements, which leads to increased agarose concentrations and thus stiffer gels .
[26] A. Pandey, C. L. Nawijn, and J. H. Snoeijer, Europhys. Lett. **122**, 36006 (2018).
[27] S. Mora, T. Phou, J.-M. Fromental, and Y. Pomeau, Phys. Rev. Lett. **113**, 178301 (2014).
[28] J. B. Pendry, Phys. Rev. Lett. **85**, 3966 (2000).
[29] S. Brûlé, E. H. Javelaud, S. Enoch, and S. Guenneau, Phys. Rev. Lett. **112**, 133901 (2014).
[30] J. D. Eshelby, Proc. R. Soc. London Ser. A: Math. Phys. Sci. **241**, 376 (1957).
[31] F. Chati, F. Léon, D. Décultot, and G. Maze, J. Acoust. Soc. Am. **129**, 1899 (2011).